



Cite this: *RSC Adv.*, 2020, 10, 26604

# Investigation of the structural, optical and gas sensing properties of PANI coated Cu–ZnS microsphere composite†

Hemalatha Parangusan,<sup>a</sup> Jolly Bhadra,<sup>a</sup> Zubair Ahmad,<sup>a</sup> <sup>a</sup> Shoaib Mallick,<sup>b</sup> Farid Touati<sup>b</sup> and Noora Al-Thani<sup>b</sup> <sup>\*a</sup>

Polyaniline (PANI)/Cu–ZnS composites with porous microspheres are prepared by a hydrothermal and *in situ* polymerization method. The structural, optical, and morphological properties are characterized by X-ray powder diffraction, FTIR, UV-vis, scanning electron microscope, transmission electron microscope. The XRD results confirmed that the PANI/Cu–ZnS composite is formed. The morphological analyses exhibited that the PANI/Cu–ZnS composite comprises the porous microspherical structures. The emission peaks obtained in photoluminescence spectra confirm the presence of surface defects in the prepared composite. The UV-DRS study shows that the bandgap of the samples is found to decrease for the PANI/Cu–ZnS composite compared to the pure Cu–ZnS sample. The calculated band gap ( $E_g$ ) value of PANI/Cu–ZnS composite is 2.47 eV. Furthermore, the fabricated gas sensor based on PANI/Cu–ZnS can perform at room temperature and exhibits good gas sensing performance toward CO<sub>2</sub> gas. In particular, PANI/Cu–ZnS sensor shows good response (31 s) and recovery time (23 s) upon exposure to CO<sub>2</sub> gas. The p/n heterojunction, surface defects, and porous nature of the PANI/Cu–ZnS composite microsphere enhanced sensor performance.

Received 5th June 2020  
Accepted 24th June 2020

DOI: 10.1039/d0ra04991c

rsc.li/rsc-advances

## 1. Introduction

Carbon dioxide (CO<sub>2</sub>) is one of the primary greenhouse gases; this leads to an adverse effect on the environment such as global warming and climate change. Therefore, the detection and monitoring of this gas are necessary to maintain a healthy environment. CO<sub>2</sub> sensors are widely used in many applications such as air-quality monitoring, food packaging, greenhouse-gas monitoring, medical diagnosis, fire detection, and consumer electronics.<sup>1–3</sup> Another crucial requirement for monitoring the level of CO<sub>2</sub> is found inside the greenhouse, where the growth of plants is directly dependent on the CO<sub>2</sub> concentration. Therefore, regulation and monitoring of the CO<sub>2</sub> level is also important in the agriculture industry.

Recently, inorganic materials have been extensively used for gas sensor applications owing to their excellent performance, such as good response and gas selectivity.<sup>4</sup> Among the semiconductors, ZnS is an n-type semiconductor and most systematically investigated semiconductors and find considerable applications in several fields such as field emitters, lasers,

phosphors, solar cells, and gas sensors.<sup>5–9</sup> It is well known as an II–VI metal sulfide semiconductor exhibiting a wide direct bandgap, good thermal stability, excellent transport properties, and presence of polar surfaces.<sup>10</sup> However, most ZnS shows disadvantages such as a low response and sensitivity at room temperature. It needs a high working temperature to enhance gas sensing performance. At higher temperatures, ZnS easily oxidizes to ZnO and decreasing sensor performance.<sup>11</sup> Composite materials based on conducting polymer and semiconductors have been extensively utilized to enhance the performance of gas sensing at room temperature.<sup>12</sup> Polyaniline (PANI) has been widely investigated p-type conducting polymer due to its excellent characteristics such as favorable optical and electrical properties, change in conductivity, and ability to work at room temperature.<sup>13</sup> PANI based composites for the gas sensor are synthesized and reported by quite a few researchers. The PANI-PVA composites have been reported for the carbon dioxide sensing by Doan *et al.*<sup>14</sup> PANI/titanium dioxide nanocomposites and PANI/sodium superoxide composite showed high sensitivity toward the CO<sub>2</sub> sensor, and the fabricated sensor shows good response and recovery time.<sup>15,16</sup>

Moreover, the hollow micro/nano-structured materials help to enhance the gas sensor performance, owing to their unique architecture, high surface to volume ratio, low density, good surface permeability, and well-defined interior voids. Therefore, the micro/nano hollow structured materials have been considered as an ideal candidate for gas sensor applications.<sup>17</sup> Wang

<sup>a</sup>Centre for Advanced Materials (CAM), Qatar University, P.O. Box 2713, Doha, Qatar. E-mail: n.al-thani@qu.edu.qa

<sup>b</sup>Department of Electrical Engineering, College of Engineering, Qatar University, P.O. Box 2713, Doha, Qatar

† Electronic supplementary information (ESI) available. See DOI: 10.1039/d0ra04991c



*et al.*<sup>18</sup> have demonstrated that a hollow microstructure improves the performance of gas sensors. The porous microstructure for gas sensing has been reported by Jian Wang *et al.*, and it showed excellent sensitivity.<sup>19</sup> Liu *et al.*<sup>20</sup> synthesized porous nano/microspheres by a facile one-step solvothermal process method, which was suitable for the gas sensors.

Bacaksız *et al.*<sup>21</sup> have fabricated Cu-doped ZnS thin films, and they have measured the charge carrier type by using Hall measurements, and it was found to be n-type. They have reported that the concentration of Cu-ions influences the charge carrier type in ZnS based materials. In this work, we have synthesized Cu-doped ZnS with a very low concentration of Cu. Hydrothermal method is used to prepare Cu-ZnS microsphere and PANI/Cu-ZnS porous microspheres are successfully prepared by *in situ* polymerization method, where the PANI is the key parameter for the formation of porous microstructure. The sensor performance of pure and PANI/Cu-ZnS composite are investigated. The sensing results indicated that the PANI/Cu-ZnS composite has a higher sensor response upon exposure of CO<sub>2</sub> gas at room temperature. At the same time, the enhanced sensing is also discussed in terms of the p/n heterojunction and porous microstructure of the core-shell structure.

## 2. Experimental

### 2.1. Materials

Aniline, hydrochloric acid (HCl) and ammonium persulfate (APS) are purchased from Sigma Aldrich. Zinc acetate dehydrate, cupric acetate, thiourea, and polyethylene glycol (PEG) are used for the synthesis of Cu doped ZnS. All the chemicals are obtained from Sigma Aldrich.

### 2.2. Synthesis of Cu-ZnS microsphere via hydrothermal method

Cu-doped ZnS microspheres are synthesized with one wt% of Cu. Zinc acetate and cupric acetate are dissolved in 50 ml distilled water. Then, 1 g thiourea is added with continuous stirring. In addition to that, 0.5 g PEG is added as a capping agent. Then, the mixture solution is immediately transferred into a 100 ml Teflon-lined stainless-steel autoclave and then subjected to heat at 160 °C for 3 h. The resultant precipitate is collected by filtration and washed with distilled water and ethanol. Subsequently, they left it to dry at 60 °C in a vacuum oven.

### 2.3. Synthesis of PANI/Cu-ZnS composite

Fig. 1a illustrates the synthesis of PANI/Cu-ZnS composites by our previously reported polymerization method.<sup>22</sup> Briefly, the polymerization of aniline is carried out at below 5 °C in an ice bath. Then, the prepared Cu-ZnS microsphere is immersed in a 0.01 M HCl solution containing aniline. Ammonium persulfate is added dropwise to the solution of aniline to initiate the polymerization and stirring for 24 h. Finally, the resultant precipitate is washed several times with deionized water and ethanol. Subsequently, the precipitate is dried at 60 °C in a vacuum oven.

### 2.4. Characterization methods

The phase structure of the samples is determined by a powder X-ray diffractometer (Empyrean, Panalytical, UK). The surface morphologies of the samples are examined using a Scanning Electron Microscope (Nova Nano SEM 450) and Transmission

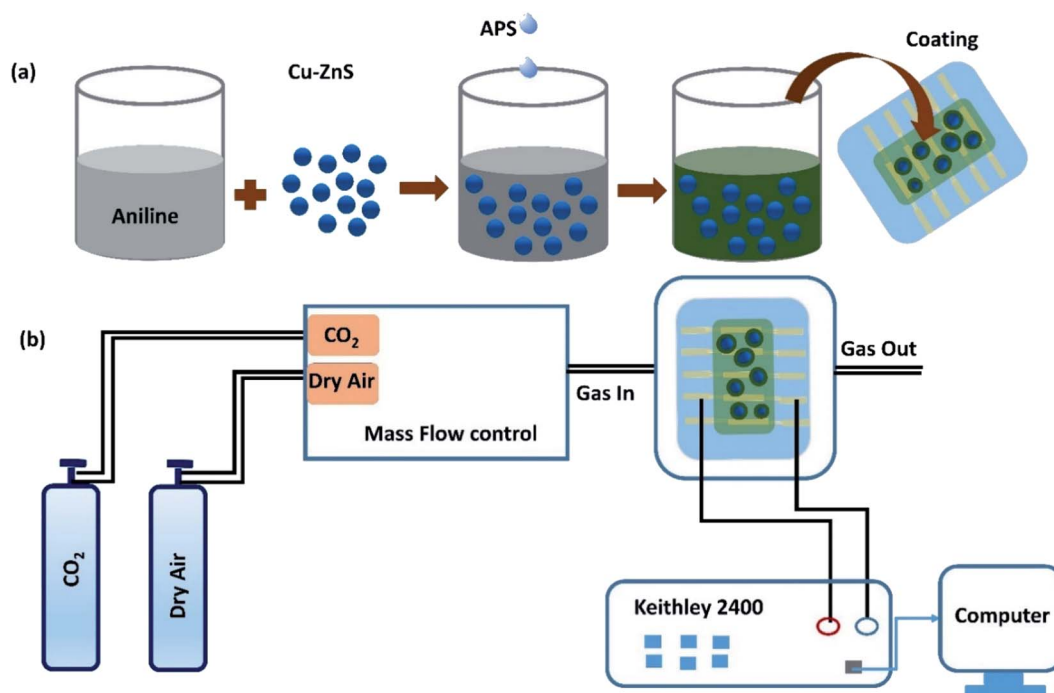


Fig. 1 (a) Illustrates the preparation of PANI/Cu-ZnS composite thin film, (b) schematic representation of gas sensor measurement.

Electron Microscope (TEM) (Philips CM 12). The Fourier transform infrared (FTIR) spectrum is recorded with PerkinElmer Spectrum 400 spectrophotometer in the range 400–400  $\text{cm}^{-1}$ . The thermal properties are analyzed by a PerkinElmer thermogravimetric analysis (TGA) (4000). Biocrom Libra S 70 spectrophotometer used to record UV-vis absorbance spectra. For the fabrication of the sensor, re-patterned interdigitated ITO (Indium tin oxide)/glass substrates (S161) are purchased from Ossila. The thickness of ITO on the glass substrate is 100 nm. Each substrate with dimensions (20 mm  $\times$  15 mm) (ESI file†) consists of the 5 ITO based interdigitated sensation electrodes, while each interdigitated sensation electrode comprises of three channels with size of 30 mm  $\times$  50  $\mu\text{m}$ . Before coating the sensing materials, the ITO/glass substrate is cleaned sequentially in acetone and deionized water in an ultrasonicator bath for 10 min.

Finally, the surface of the ITO is dried by nitrogen blow. To deposit the sensing film, the PANI/Cu–ZnS (200 mg) composite is first dispersed into 2 ml of ethanol. Then the solution is spin-coated onto the substrate at 5000 rpm for 60 s and dried at 60  $^{\circ}\text{C}$  for 1 h. For dispersion of composite powder in the ethanol, we followed the Hao Juanyuan *et al.*<sup>23</sup> For spinning time and velocity, our group has already optimized the spinning time and spinning velocity of nanocomposite-based sensing film.<sup>24</sup> The thickness of the PANI/Cu–ZnS composite films were recorded using profilometer (LEICA DCM8) and the average thickness was found to be  $417 \pm 20$  nm (see the table in the ESI file†). The surface area of the sensing layer was 30 mm  $\times$  150  $\mu\text{m}$ . The

sensor fabrication processes are schematically represented in Fig. 1a. Gas sensing properties are tested by using an assembled experimental set up.<sup>25</sup> The set up included Keithley 2400, source meter, measuring chamber, and measuring devices. The Keithley 2400 measured the electrical properties of the fabricated sensors. Fig. 1b shows the experimental set up for sensor measurement.

### 3. Result and discussion

#### 3.1. Morphological properties of PANI/Cu–ZnS composites

Fig. 2a demonstrates the PANI coated Cu–ZnS hollow microsphere synthesis *via* hydrothermal and *in situ* polymerization procedures. The morphology and crystalline structures are examined using a scanning electron microscope (SEM) and X-ray powder diffraction studies, respectively. The SEM image in Fig. 2b shows the porous microstructure morphology of the PANI/Cu–ZnS composites. The pure Cu–ZnS shows the microsphere structure inset in Fig. 2b.

In the case of pure Cu–ZnS, the SEM image shows the solid microspheres, but no porous spheres are formed (inset Fig. 2b). However, in the case of PANI/Cu–ZnS composites, we can see that a part of spheres was etched and very small voids appeared on each sphere of Fig. 2b, which indicates that the PANI is a key parameter for the formation of porous structures. The well-constructed porous microsphere contributed to the large specific surface area that is beneficial for the enhancement of gas sensitivity.<sup>26</sup>

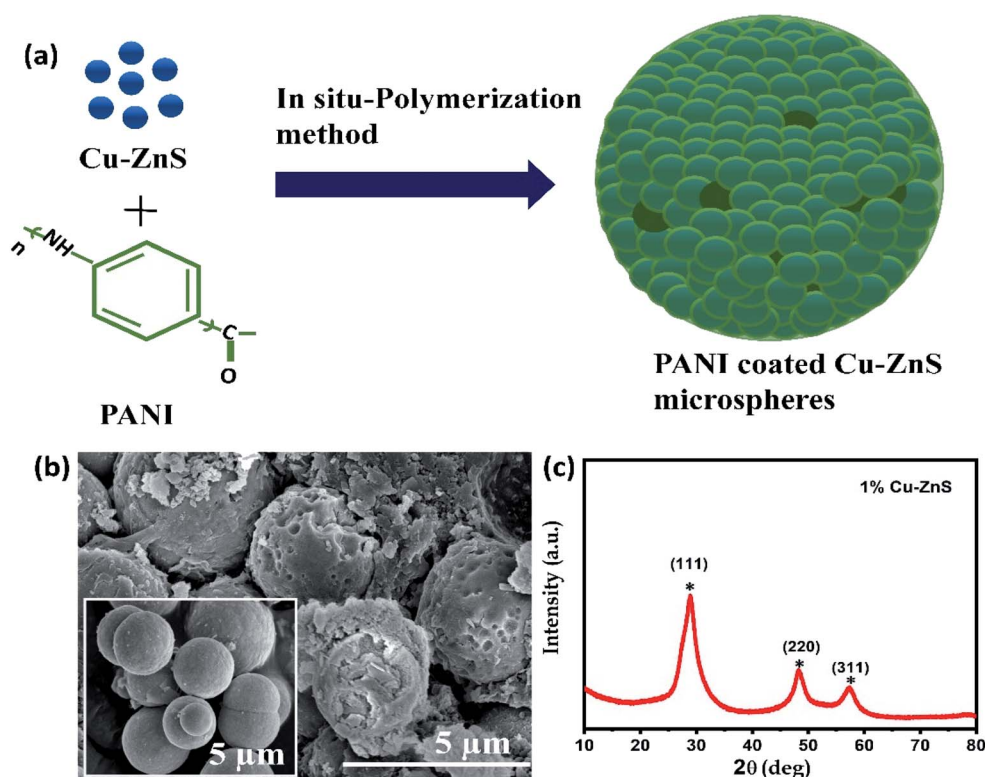


Fig. 2 (a) Schematic representation of synthesis process, (b) SEM images of PANI/Cu–ZnS (inset Cu–ZnS), (c) X-ray diffraction pattern of Cu–ZnS.



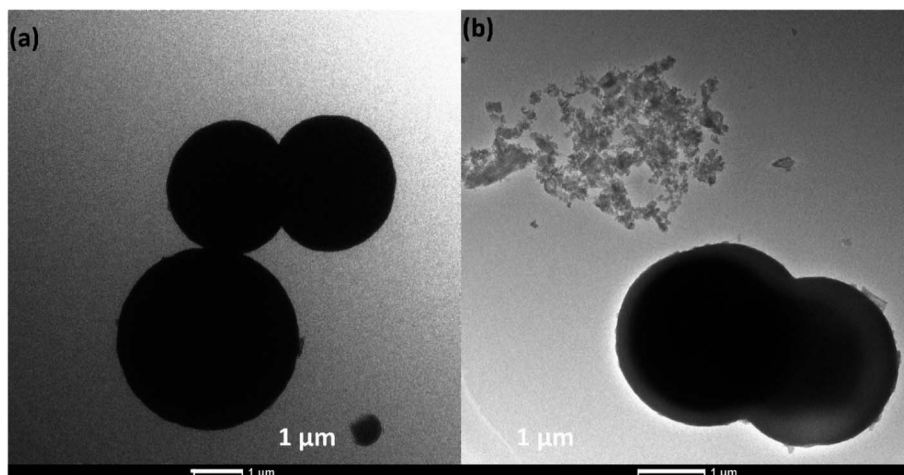


Fig. 3 (a) TEM images of pure Cu-ZnS, (b) PANI/Cu-ZnS composite.

The X-ray diffraction pattern of pure Cu-ZnS is shown in Fig. 2c. The Cu-ZnS show the main diffraction peaks at  $2\theta$  values  $28.6^\circ$ ,  $48.2^\circ$  and  $57.3^\circ$  correspond to the crystalline planes of (111), (220), and (311), respectively (ZnS with cubic structure, JCPDS no. 05-0566). As can be seen from Fig. 2c, there is no diffraction peaks originating from Cu and other impurities in XRD-data, which indicates that the dopant is substituted into the lattice sites during the synthesis process.<sup>27</sup> The present study demonstrates that the incorporation of  $\text{Cu}^{2+}$  ions in ZnS lattice suppresses the growth of crystallite size. Substitution of  $\text{Cu}^{2+}$  ion in ZnS lattice could replace either the substitutional or interstitial zinc ions in the ZnS lattice that would result in structural deformation. Also, researchers reported that the addition Cu ions introduces some additional energy levels, which are close to the valence band edge in the bandgap of host ZnS. The tuning of the bandgap energy by the Cu dopant is desirable for optoelectronic devices, solar cells, and detector applications. Hence, the overlap of the  $\text{Cu}^{2+}$  ion and  $\text{Zn}^{2+}$  ion could enhance the gas sensing performance.

The surface morphologies of the samples are further analyzed by using transmission electron microscopy (TEM). Fig. 3a shows the TEM image of pure Cu-ZnS, which showed microsphere structures. Fig. 3b shows the TEM image of PANI/Cu-ZnS composite, indicating that the PANI is coated on the surface of the Cu-ZnS microsphere.

It looks like a core-shell structure with a gray shell, and bright core is observed for the PANI/Cu-ZnS composite. This is attributed to the presence of a hollow space that enhances the contrast between the Cu-ZnS core and PANI shell.<sup>28</sup> The SEM and TEM results concluded that the incorporation of PANI results in the synthesis of a complex mixture of porous and core/shell microspheres.

### 3.2. Structural and thermal properties of PANI/Cu-ZnS composites

The X-ray diffraction patterns of pure PANI and PANI/Cu-ZnS composites are shown in Fig. 4a. The diffraction peaks at  $14.4^\circ$ ,

$20.5^\circ$ , and  $25.3^\circ$  corresponding to (011), (020), and (200) crystalline planes of pure PANI, respectively.<sup>29</sup>

The XRD pattern of PANI/Cu-ZnS shows strong PANI and Cu-ZnS diffraction peaks. No extra peaks of other impurities are detected in the XRD pattern, which indicates the PANI/Cu-ZnS composite is formed.

Fig. 4b shows the TGA curves of pure PANI, Cu-ZnS, and its composites. TGA is used to investigate the thermal stability of the material and to test the higher temperature applicability of the composites. ZnS based gas sensors are rigid and operated at elevated temperatures. These features may prohibit the application of room temperature based gas sensor. To reduce the operating temperature of ZnS based sensors, it is combined with some conducting polymers.<sup>30</sup> The combination of ZnS and PANI composite material is suitable for the application of room temperature based gas sensors. Also, it improves the optical and thermal properties of the material. As shown in Fig. 4b, the thermal stability of Cu-ZnS is high, and very negligible weight loss is observed. The pure PANI shows three-step weight loss is observed, and it is shown in Fig. 3b. The first weight loss in the first step at  $70^\circ\text{C}$  and it is mainly due to the expulsion of moisture present in the composite.<sup>31</sup> The weight loss in the temperature range of  $220^\circ\text{C}$  is due to the removal of dopant molecules, and the third weight loss is due to the degradation of the polymer backbone.<sup>32</sup> The thermal stability of PANI/Cu-ZnS composite is in between that of pure PANI and Cu-ZnS, *i.e.*, higher than that of pure PANI and lower than that of Cu-ZnS, owing to the strong interaction between Cu-ZnS and PANI. The thermal stability of pure PANI is less than the composite. Thus, Cu-ZnS incorporation leads to increase the thermal stability of the PANI/Cu-ZnS composite is a useful sensor for gas detection.

FTIR Spectroscopy is used to investigate the chemical structure of pure Cu-ZnS, PANI, and PANI/Cu-ZnS composite. Fig. 4c shows the FTIR spectra of Cu-ZnS, PANI and PANI/Cu-ZnS composites. The FTIR spectrum of pure PANI shows the peaks at  $1547\text{ cm}^{-1}$ , and  $1468\text{ cm}^{-1}$  corresponds to the  $\text{C}=\text{N}$  and  $\text{C}=\text{C}$  stretching vibrations of quinonoid and benzenoid



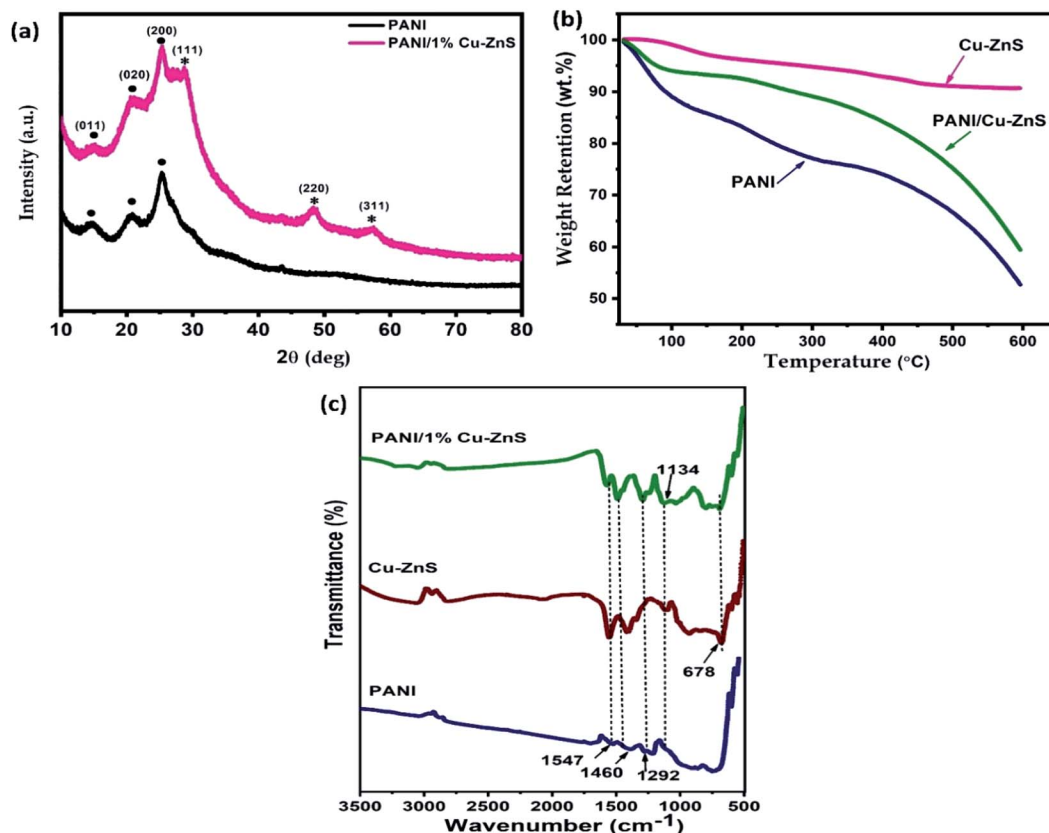


Fig. 4 (a) XRD pattern, (b) TGA analysis, and (c) FTIR spectra of pure PANI and PANI/Cu–ZnS composite.

rings of PANI.<sup>33</sup> The peak observed at  $1292\text{ cm}^{-1}$  can be ascribed to the  $\text{C-H}$  out of plane bending vibration. The peak exhibited at  $1134\text{ cm}^{-1}$  indicates the formation of the doped polymer.<sup>34</sup> In the pure Cu–ZnS sample, the peak found at  $678\text{ cm}^{-1}$  is attributed to the stretching vibrations of Zn–S bonds.<sup>35</sup> In the FTIR spectrum of PANI/Cu–ZnS composites, the main peaks for PANI and Cu–ZnS can be observed. These results indicate that there is intermolecular interaction between the Cu–ZnS and polyaniline matrix.

### 3.3. UV-vis absorbance studies

UV-vis absorption measurements are performed to investigate the defect energy levels in the bandgap of the porous composite materials. The optical absorption properties of the samples are recorded in the range of 220–900 nm by UV-vis spectrophotometer and is shown in Fig. 5a and b. Pure Cu–ZnS demonstrated a characteristic peak around 200–350 nm in UV-region. The characteristic bands of pure PANI showed absorbance bands in both UV and IR-region. In the UV region, the

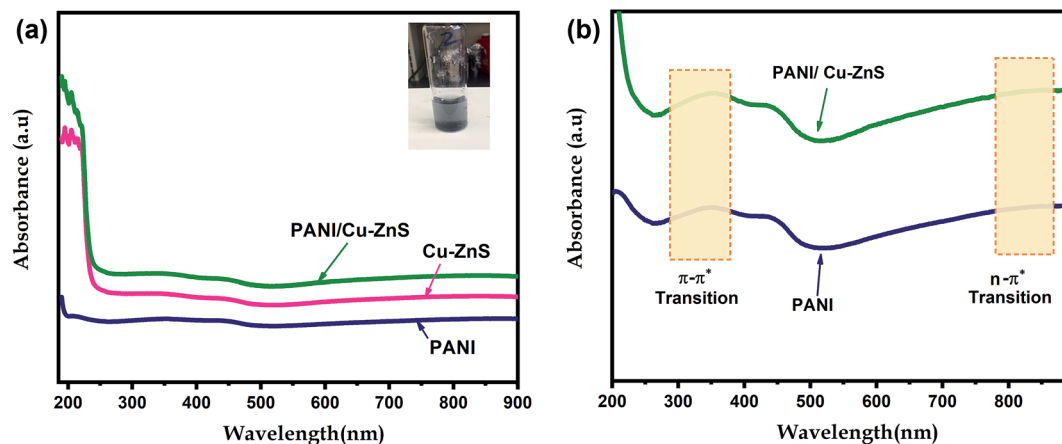


Fig. 5 The optical absorption spectrum of (a) pure PANI, Cu–ZnS and PANI/Cu–ZnS composite, (b) the absorption bands of PANI and PANI/Cu–ZnS in the UV and IR region.



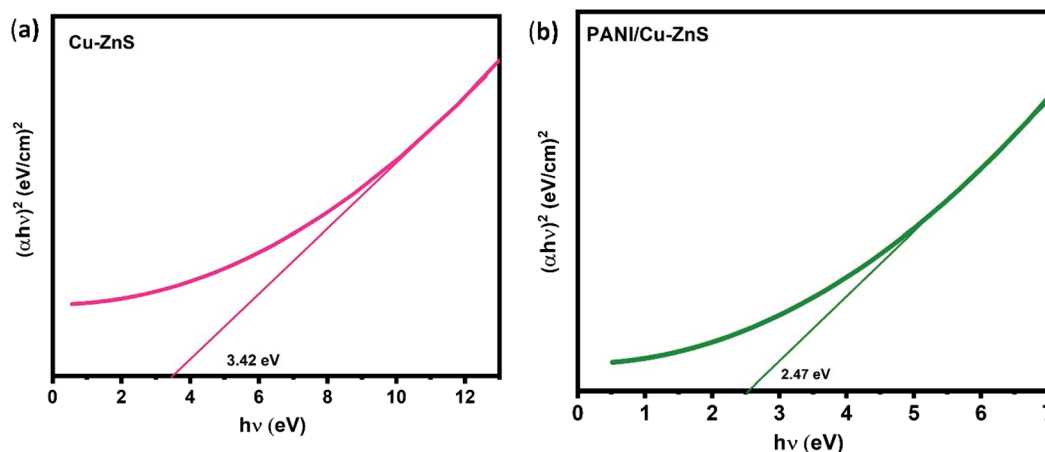


Fig. 6 Tauc's plot of (a) pure Cu-ZnS, (b) PANI/Cu-ZnS composite.

characteristics peak at 200–470 nm due to the  $\pi$ - $\pi^*$  transition of the benzenoid ring. In the visible region, the absorbance band at 490–730 nm, which is due to the benzenoid ring to quinoid ring ( $n$ - $\pi^*$  transition).<sup>36</sup> In the case of PANI/Cu-ZnS composites, showed both PANI and Cu-ZnS characteristics absorption bands. As shown in Fig. 5b, the characteristic peak of  $\pi$ - $\pi^*$  benzenoid ring found to be red-shifted for the PANI/Cu-ZnS composite than the pure Cu-ZnS, which is due to the interaction between Cu-ZnS and PANI. This observation further supports the formation of PANI/Cu-ZnS composite. The interaction between PANI and Cu-ZnS can facilitate the electron-transfer process in the composites and results in improving the conductivity in the polymer composites.<sup>37</sup>

The optical band gap energy ( $E_g$ ) of the composite is determined from the absorption spectra using the following equation.<sup>38</sup>

$$(\alpha h\nu)^n = A(h\nu - E_g) \quad (1)$$

where  $\alpha$  is the absorption coefficient,  $h\nu$  the photon energy, and  $A$  is constant. The exponent ' $n$ ' can assign values of 1/2, 2, 3/2, and 3, respectively. It is equal to 1/2 and 2 for the allowed direct and indirect transition. But,  $n$  takes the values of 3/2 for the direct forbidden transition and 3 for the indirect forbidden transitions, respectively. Tauc's plots are used to calculate the bandgap of the samples. Tauc's plot is shown in Fig. 6a and b.

The graph is drawn between  $(\alpha h\nu)^2$  versus  $h\nu$ .  $E_g$  value is obtained as the plot tangent intercept at the X-axis. The calculated energy bandgap for pure Cu-ZnS and PANI/Cu-ZnS composite are found to be 3.42 eV and 2.47 eV. The bandgap is decreased for the PANI/Cu-ZnS composite than the pure Cu-ZnS. This is due to the substitution of PANI into Cu-ZnS. The band-gap narrowing of the material improves the gas adsorption and desorption to accelerate the reaction rate.<sup>39</sup> The calculated band gap values of the samples are higher than that of the bulk ZnS. This is due to the confinement of electrons and holes; the lowest energy optical transition from the valence to the conduction band will increase in energy.<sup>40</sup>

### 3.4. Photo luminescence spectra

Fig. 7 shows the luminescence spectra of PANI/Cu-ZnS composite at an excitation wavelength of 250 nm. The composite shows emission at near band edge emission (NBE) in the UV region and defect level emission (DLE) in the visible region. The near band emission is obtained around 354 nm can be attributed to the radiative recombination of free excitons through the exciton-exciton collision process.<sup>41</sup> The visible defect level emission band observed at 423 nm is attributed to a blue emission band. The blue emission is assigned to the defect states in the PANI/Cu-ZnS composite, which is associated with the oxygen vacancies.<sup>42</sup> The more oxygen vacancies is beneficial for the enhancement of gas sensitivity.<sup>43</sup>

### 3.5. Gas sensing properties

The gas sensing behavior of the PANI/Cu-ZnS composite for carbon dioxide gas at room temperature is investigated, and their dynamic response curves for 80 ppm CO<sub>2</sub> at room temperature are shown in Fig. 8a–d. It is noted that the pure

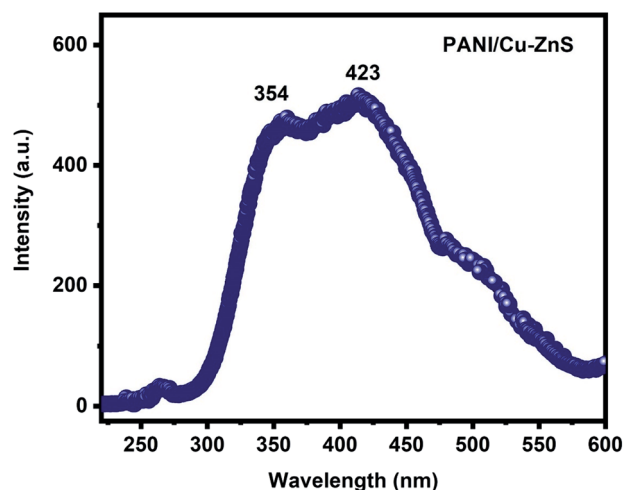


Fig. 7 Luminescence spectra of PANI/Cu-ZnS composite.



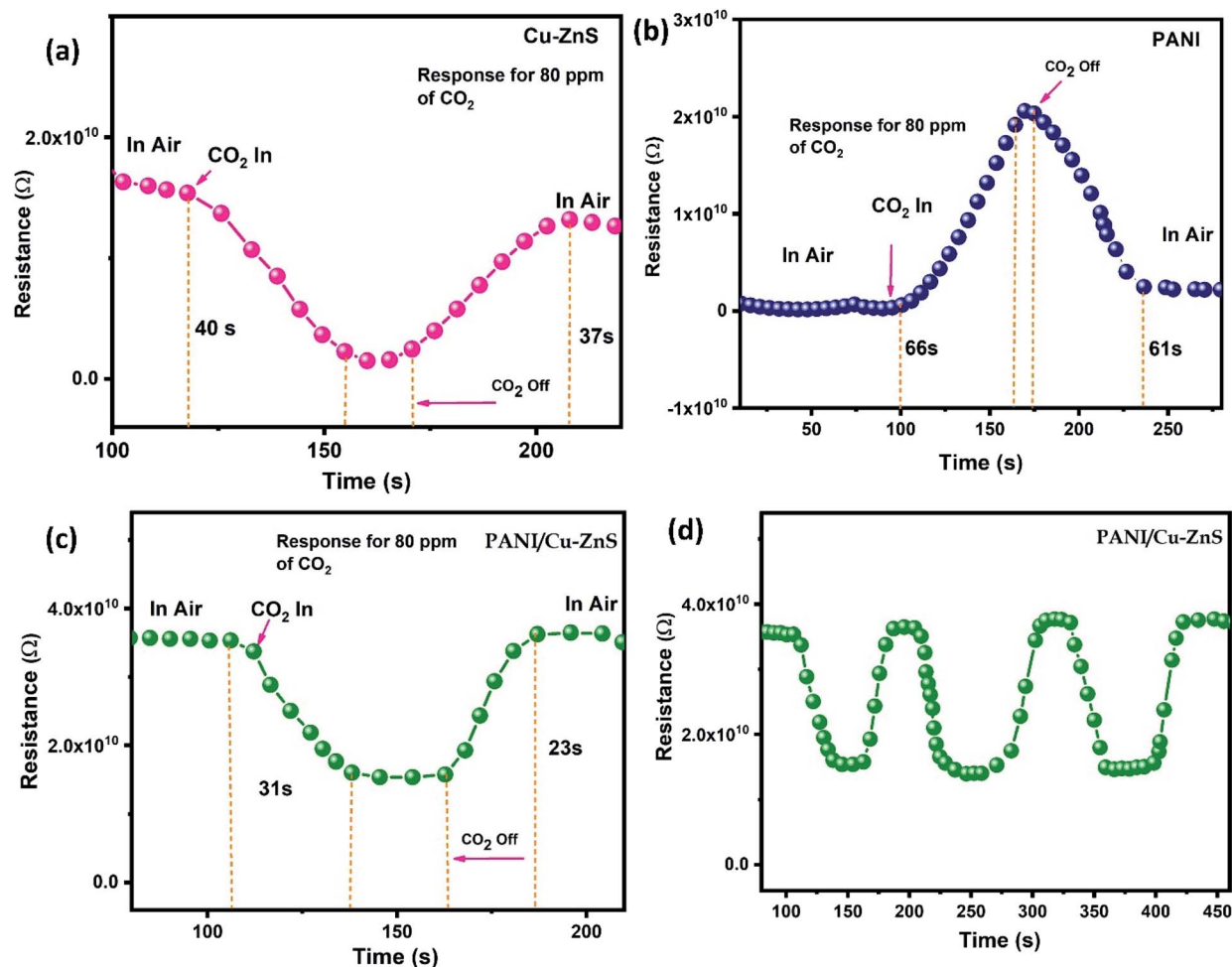


Fig. 8 Gas sensing response of (a) pure Cu-ZnS, (b) pure PANI, (c) PANI/Cu-ZnS composite, (d) Repeatability curve of PANI/Cu-ZnS composite at room temperature.

PANI showed a typical p-type sensing behavior (Fig. 8b), both Cu-ZnS and PANI/Cu-ZnS exhibit n-type sensing behavior (Fig. 8a and c).

From Fig. 8a and c, when CO<sub>2</sub> has injected the sensor resistances decrease and then reach stable values. When gas supply is stopped, the resistances will increase and finally return to their baselines. The improved sensing signal of PANI/Cu-ZnS composite is due to the p-n heterojunction of PANI and Cu-ZnS core-shell structure.<sup>44</sup>

Generally, the response time is defined as the time taken to reach 90% of the steady-state value after the CO<sub>2</sub> is injected, whereas the recovery time is defined as the time needed for the sensor to recover over 90% of the maximum sensitivity. The sensing response and recovery times for the PANI/Cu-ZnS composite are 31 s and 23 s, respectively. A comparison of CO<sub>2</sub> sensing properties of our material and literature reported sensor is shown in Table 1. The enhanced sensing behavior of PANI/Cu-ZnS composite is due to the porous microsphere; it is easy for gas molecules to diffuse from all the directions. In addition, surface defects play a crucial role in the enhancement of sensing performance. It

is evident from the SEM, TEM, and luminescence results. Fig. 8d shows the repeatability of the fabricated PANI/Cu-ZnS sensor. The results indicate that the fabricated sensor has good repeatability.

**3.5.1 Gas sensing mechanism.** In general, the improved gas sensing properties of organic-inorganic composite is explained based on nanostructured materials. Cao *et al.*<sup>50</sup> have suggested that the increment in the response magnitude not only due to the increased specific surface area of

Table 1 CO<sub>2</sub> gas sensing properties of PANI/Cu-ZnS composite compared with previous work

Materials	Response time	Recovery time	Ref.
NBA-ZnS nanohybrids	206 s	354 s	3
PEDOT-BPEI	13 min	30 min	45
Polymerized polypyrrole	210 s	1100 s	46
TiO <sub>2</sub> -PANI	9.2 min	5.7 min	47
Ag-BaTiO <sub>3</sub> -CuO	15 min	10 min	48
CuO-Cu <sub>2</sub> Fe <sub>3</sub> -xO <sub>4</sub>	9.5 h	—	49
PANI/Cu-ZnS	31 s	23 s	This work



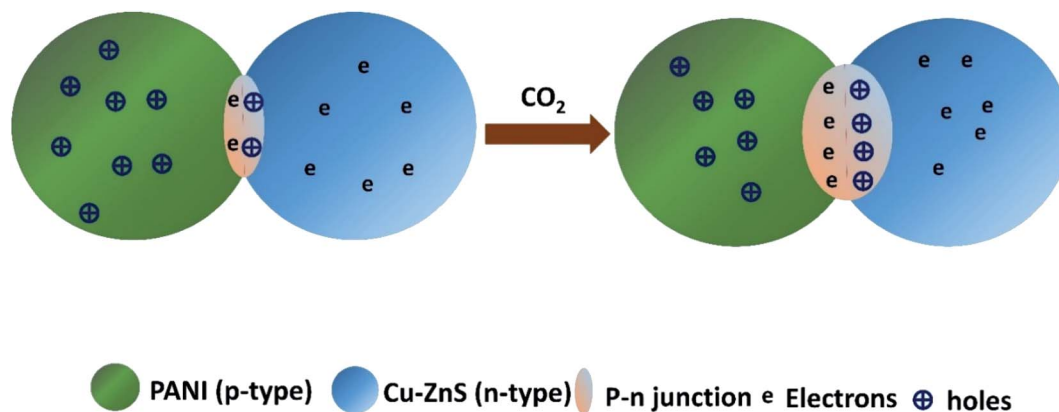


Fig. 9 Schematic illustration of gas sensing mechanism.

nanostructures. Even otherwise, it can be due to the formation of p/n junction between p-type and n-type materials played an important role in improving the response magnitude of the inorganic/organic nanocomposites. In the case of 1D nanofibers,  $\text{SnO}_2$ , and  $\text{TiO}_2$ /polypyrrole composites prepared by Wang *et al.*,<sup>51</sup> the origin of higher response magnitude is explained by the p/n junction theory. Further, it has been stated by Li *et al.*<sup>12</sup> that the porous structure with a larger specific surface area helps to improve the sensing properties. In addition, the presence of surface defects also led to increasing the sensing performance because the surface defects facilitate more adsorption sites for gas adsorption.<sup>52</sup> Therefore, it is concluded that the porous microstructure, p/n heterojunction and surface defects are an important factor for the enhancement of sensing performance.

In our case, p-type PANI and n-type Cu-ZnS in composite formed a p-n heterojunction at the interface, which would increase the sensing response. In addition, the porous structure can provide more active sites and be beneficial to adsorption and diffusion of gas molecules and its dynamicity.  $\text{CO}_2$  gas sensing mechanism can be understood by schematic representation shown in the Fig. 9. The mechanism for the good sensing performance of PANI/Cu-ZnS composite can be explained as follows, when the sensor surface exposes to air, oxygen molecules is adsorbed on the surface of the porous structure and capture free electrons from the conduction band of Cu doped ZnS. Then the adsorbed oxygen will form the chemisorbed oxygen species, which turns to an electron depletion layers form at the surface of the composite material. When PANI/Cu-ZnS surface is exposed to the  $\text{CO}_2$  gas, the gas molecules will capture holes from the PANI. Then the depletion layers of p-n junctions are extended, which would increase the resistance of the sensor. The change in the resistance is due to the adsorbed gas molecules on the surface of the PANI/Cu-ZnS composite sensor. When the film is exposed to carbon dioxide gas at the operating room temperature, the gas molecules react with the pre-adsorbed oxygen species on the surface of the sensor. As a result, the surface oxygen concentration is reduced, and electrons that were initially trapped by oxygen anions are released back into the valence band, which recombine with the

holes and decrease the charge carrier (hole) concentration, leading to an increase in the resistance of the PANI/Cu-ZnS composite sensor. Moreover, the PANI/Cu-ZnS composite sensor shows fast response and recovery time to  $\text{CO}_2$  gas. This could be due to the presence of p-type PANI and n-type Cu-ZnS, which gives a superior carrier transport path in the PANI/Cu-ZnS composite sensor.<sup>53</sup>

## 4. Conclusion

In summary, PANI/Cu-ZnS porous microstructure is synthesized by the hydrothermal method and *in situ* polymerization process. The prepared PANI/Cu-ZnS composite possesses porous microstructure, p/n heterojunction, and surface defects, which helps to improve the gas sensing properties of the prepared samples. The presence of oxygen vacancies is confirmed from the luminescence spectra, which enhances the sensing performance. From the gas sensing results, it is concluded that the PANI/Cu-ZnS based gas sensor showed good sensing performance towards 80 ppm carbon dioxide gas at room temperature. Also, the porous microsphere composite exhibits quick response and recovery behavior and good reproducibility, indicating their promising application as gas sensing materials. The response and recovery times are as 31 s and 23 s upon exposure to  $\text{CO}_2$  gas. Thus, it can be concluded that PANI/Cu-ZnS porous microstructure composite based gas sensor is a good candidate for room temperature carbon dioxide sensing.

## Conflicts of interest

There are no conflicts of interest to among the authors.

## Acknowledgements

This work is supported by Qatar University Internal Grant No. QUCG-CAM-2019-1. The findings achieved herein are solely the responsibility of the authors. The characterizations of this work are accomplished in the Central Laboratories Unit, Qatar University.





## References

- 1 J. Zosel, W. Oelbner, M. Decker, G. Gerlach and U. Guth, *Meas. Sci. Technol.*, 2011, **22**, 072001.
- 2 S. B. Jagadale, V. L. Patil, S. A. Vanalakar, P. S. Patil and H. P. Deshmukh, *Ceram. Int.*, 2018, **44**, 3333–3340.
- 3 B. Mandal, A. Biswas, D. S. Sharma, R. Bhardwaj, M. Das, M. A. Rahman, S. Kuriakose, M. Bhaskaran, S. Sriram and M. ThanHitay, *ACS Appl. Nano Mater.*, 2018, **1**, 6912–6921.
- 4 Y. Wang, X. Cui, Q. Yang, J. Liu, Y. Gao, P. Sun and G. Lu, *Sens. Actuators, B*, 2016, **225**, 544–552.
- 5 B. Chandra, V. Chandra, P. Jha, D. Pateria and R. Baghel, *Luminescence*, 2016, **31**, 67–75.
- 6 J. Chang, T. Oshima, S. Hachiya, K. Sato, T. Toyoda, K. Katayama, S. Hayase and Q. Shen, *Sol. Energy*, 2015, **122**, 307–313.
- 7 H. Chien, C. Cheng and M.-H. Mao, *IEEE J. Sel. Top. Quantum Electron.*, 2017, **23**, 1–5.
- 8 S. Park, S. An, H. Ko, S. Lee and C. Lee, *Sens. Actuators, B*, 2013, **188**, 1270–1276.
- 9 R. Viswanath, H. Bhojya Naik, G. Arun kumar, I. Suresh Gowda and S. Yallappa, *Luminescence*, 2017, **32**, 1212–1220.
- 10 L. Zhu, Y. Wang, D. Zhang, C. Li, D. Sun, S. Wen, Y. Chen and S. Ruan, *ACS Appl. Mater. Interfaces*, 2015, **7**, 20793–20800.
- 11 F. Zhong, Z. Wu, J. Guo and D. Jia, *Sensors*, 2018, **18**, 2882.
- 12 S. Li, P. Lin, L. Zhao, C. Wang, D. Liu, F. Liu, P. Sun, X. Liang, F. Liu, X. Yan and Y. Gao, *Sens. Actuators, B*, 2018, **259**, 505–513.
- 13 C. A. Betty, S. Choudhury and S. Arora, *Sens. Actuators, B*, 2015, **220**, 288–294.
- 14 T. Doan, R. Ramaneti, J. Baggerman, J. Vander Bent, A. Marcelis, H. Tong and C. Van Rijn, *Sens. Actuators, B*, 2012, **168**, 123–130.
- 15 S. Nimkar, S. Agrawal and S. Kondawar, *Procedia Mater. Sci.*, 2015, **10**, 572–579.
- 16 R. Barde, *Mater. Res. Bull.*, 2016, **73**, 70–76.
- 17 X. Chen, X. Jing, J. Wang, J. Liu, D. Song and L. Liu, *CrystEngComm*, 2013, **15**, 7243–7249.
- 18 S. Wang, X. Gao, J. Yang, Z. Zhu, H. Zhang and Y. Wang, *RSC Adv.*, 2014, **4**, 57967–57974.
- 19 J. Wang, X. Gan, Z. Li and K. Zhou, *Powder Technol.*, 2016, **303**, 138–146.
- 20 T. Liu, J. Liu, Q. Liu, D. Song, H. Zhang, H. Zhang and J. Wang, *Nanoscale*, 2015, **7**, 19714–19721.
- 21 E. Bacaksiz, T. Dzhafarov, V. Novruzov, M. Tomakin, T. Kucukomeroglu, M. Altunbas, E. Yanmaz and B. Abay, *Phys. Status Solidi A*, 2004, **201**, 2948–2952.
- 22 J. Bhadra, N. Al-Thani, N. Madi and M. Al-Maadeed, *Synth. Met.*, 2013, **181**, 27–36.
- 23 J. Hao, D. Zhang, Q. Sun, S. Zheng, J. Sun and Y. Wang, *Nanoscale*, 2018, **10**, 7210–7217.
- 24 S. Mallick, Z. Ahmed, F. Touati, J. Bhadra, R. Shakoar and N. Al-Thani, *Ceram. Int.*, 2018, **44**, 16507–16513.
- 25 J. Bhadra, N. Al-Thani, N. Madi and M. Al-Maadeed, *J. Mater. Sci.: Mater. Electron.*, 2016, **27**, 8206–8216.
- 26 W. Koo, S. Choi, J. Jang and I. Kim, *Sci. Rep.*, 2017, **7**, 45074.
- 27 P. Hemalatha, S. Karthick, K. Hemalatha, M. Yi, H. Kim and M. Alagar, *J. Mater. Sci.: Mater. Electron.*, 2016, **27**, 2367–2378.
- 28 Q. Yue, J. Li, Y. Zhang, X. Cheng, X. Chen, P. Pan, J. Su, A. Elzatahry, A. Alghamdi, Y. Deng and D. Zhao, *J. Am. Chem. Soc.*, 2017, **139**, 15486–15493.
- 29 D. Gui, C. Liu, F. Chen and J. Liu, *Appl. Surf. Sci.*, 2014, **307**, 172–177.
- 30 M. Das and D. Sarkar, *Ceram. Int.*, 2017, **43**, 11123–11131.
- 31 T. Jeevananda, S. Seetharamu, S. Saravanan and L. Souza, *Synth. Met.*, 2004, **140**, 247–260.
- 32 R. Ansari and M. Keivani, *J. Chem.*, 2006, **3**, 202–217.
- 33 G. Khuspe, D. Bandgar, S. Sen and V. Patil, *Synth. Met.*, 2012, **162**, 1822–1827.
- 34 U. Patil, N. Ramgir, N. Kamakar, A. Bhogale, A. Bebnath, D. Aswal, S. Gupta and D. Kothari, *Appl. Surf. Sci.*, 2015, **339**, 69–74.
- 35 M. Kuppayee, G. V. Nachiyar and V. Ramasamy, *Appl. Surf. Sci.*, 2011, **257**, 6779–6786.
- 36 P. Khanna, N. Singh, S. Charan and A. Viswanath, *Mater. Chem. Phys.*, 2005, **92**, 214–219.
- 37 L. Shi, R. Liang and J. Qiu, *J. Mater. Chem.*, 2012, **22**, 17196–17203.
- 38 H. Parangusan, D. Ponnammam, M. Al-Maadeed and A. Marimuthu, *Photochem. Photobiol.*, 2018, **94**, 237–246.
- 39 F. Gao, G. Qin, Y. Li, Q. Jiang, K. Zhao, Y. Liu and H. Zhao, *RSC Adv.*, 2016, **6**, 10298–10310.
- 40 A. K. Kole and P. Kumbhakar, *Results Phys.*, 2012, **2**, 150–155.
- 41 K. Karthik, S. Dhanuskodi, C. Gobinath, S. Prabhukumar and S. Sivaramakrishnan, *J. Mater. Sci.: Mater. Electron.*, 2018, **29**, 5459–5471.
- 42 R. Chandrakar, R. Baghel, V. Chandra and B. Chandra, *Superlattices Microstruct.*, 2015, **86**, 256–269.
- 43 E. Vinoth and N. Gopalakrishnan, *Mater. Res. Express*, 2018, **5**, 066413.
- 44 L. Wang, H. Huang, Z. Xiao, D. Cai, Y. Liu, B. Liu, D. Wang, C. Wang, H. Li, Y. Wang and Q. Li, *ACS Appl. Mater. Interfaces*, 2014, **6**, 14131–14140.
- 45 C. Chiang, K. Tsai, Y. Lee, H. Lin, Y. Yang, C. Shih, C. Lin, H. Jeng, Y. Weng, Y. Cheng and K. Ho, *Microelectron. Eng.*, 2013, **111**, 409–415.
- 46 S. Waghuley, S. Yenorkar, S. Yawale and S. Yawale, *Sens. Actuators, B*, 2008, **128**, 366–373.
- 47 R. Sonker, S. Sabhajeet and B. Yadav, *J. Mater. Sci.: Mater. Electron.*, 2016, **27**, 11726–11732.
- 48 J. Herrán, G. Mandayo, I. Ayerdi and E. Castano, *Sens. Actuators, B*, 2008, **129**, 386–390.
- 49 A. Chapelle, F. Oudrhiri-Hassani, L. Presmanes, A. Barnabe and P. Tailhades, *Appl. Surf. Sci.*, 2010, **256**, 4715–4719.
- 50 Q. Xu, D. Ju, Z. Zhang, S. Yuan, J. Zhang, H. Xu and B. Cao, *Sens. Actuators, B*, 2016, **225**, 16–23.
- 51 T. Jiang, Z. Wang, Z. Li, W. Wang, X. Xu, X. Liu, J. Wang and C. Wang, *J. Mater. Chem. C*, 2013, **1**, 3017–3025.
- 52 B. Sakthivel and G. Nammalvar, *J. Alloys Compd.*, 2019, **788**, 422–428.
- 53 C. Liu, H. Tai, P. Zhang, Z. Yuan, X. Du, G. Xie and Y. Jiang, *Sens. Actuators, B*, 201, **261**, 587–597.

